Cell Reports, Volume *28*

Supplemental Information

Peptide/Receptor Co-evolution Explains the Lipolytic Function of the Neuropeptide TLQP-21

Bhavani S. Sahu, Pedro Rodriguez, Megin E. Nguyen, Ruijun Han, Cheryl Cero, Maria Razzoli, Paolo Piaggi, Lauren J. Laskowski, Mihaela Pavlicev, Louis Muglia, Sushil K. Mahata, Scott O'Grady, John D. McCorvy, Leslie J. Baier, Yuk Y. Sham, and Alessandro Bartolomucci

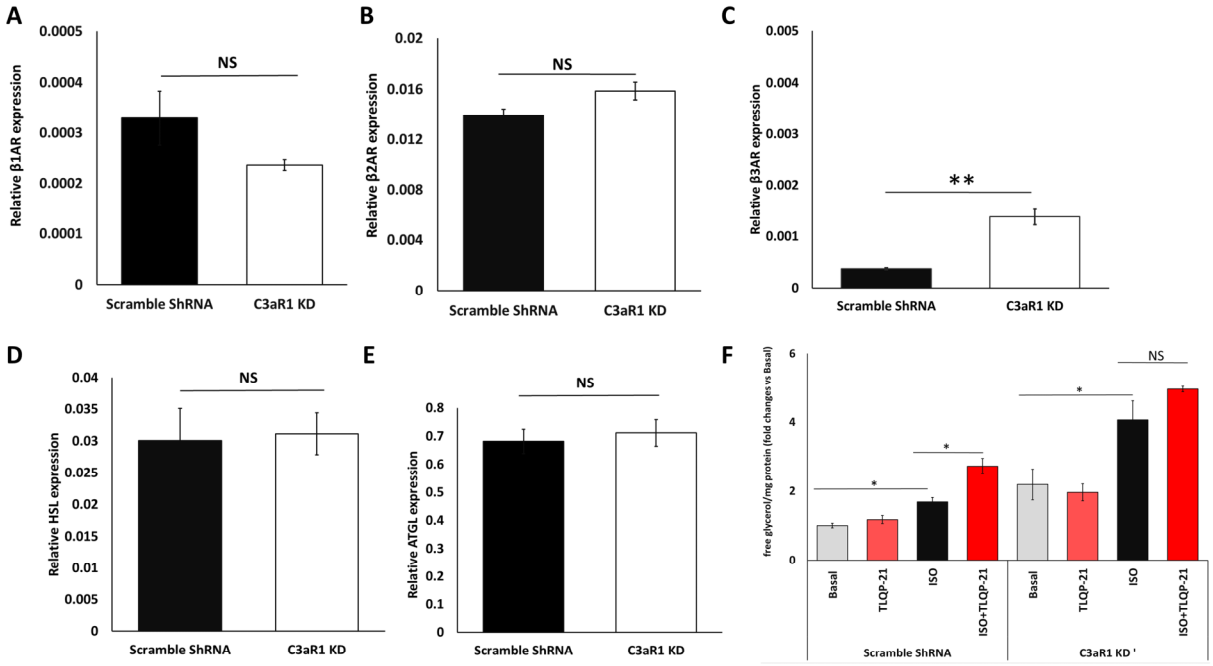

Figure S1. Characterization of C3aR1 KD cell lines, Related to Figure 1. A-E) Gene expression in non-targeting scrambled shRNA cells and C3aR1 KD cells. **F**) Free glycerol release in a second independent line of C3aR1 KD (KD') and control cells. C3aR1 KD prevents TLQP-21 (100nM) potentiation of isoproterenol (ISO, 50nM)-induced lipolysis (Cell line x treatment $F(3,58)=5.1$, $p<0.01$; N=4-14. Data from controls are the same as presented in Figure 1B).

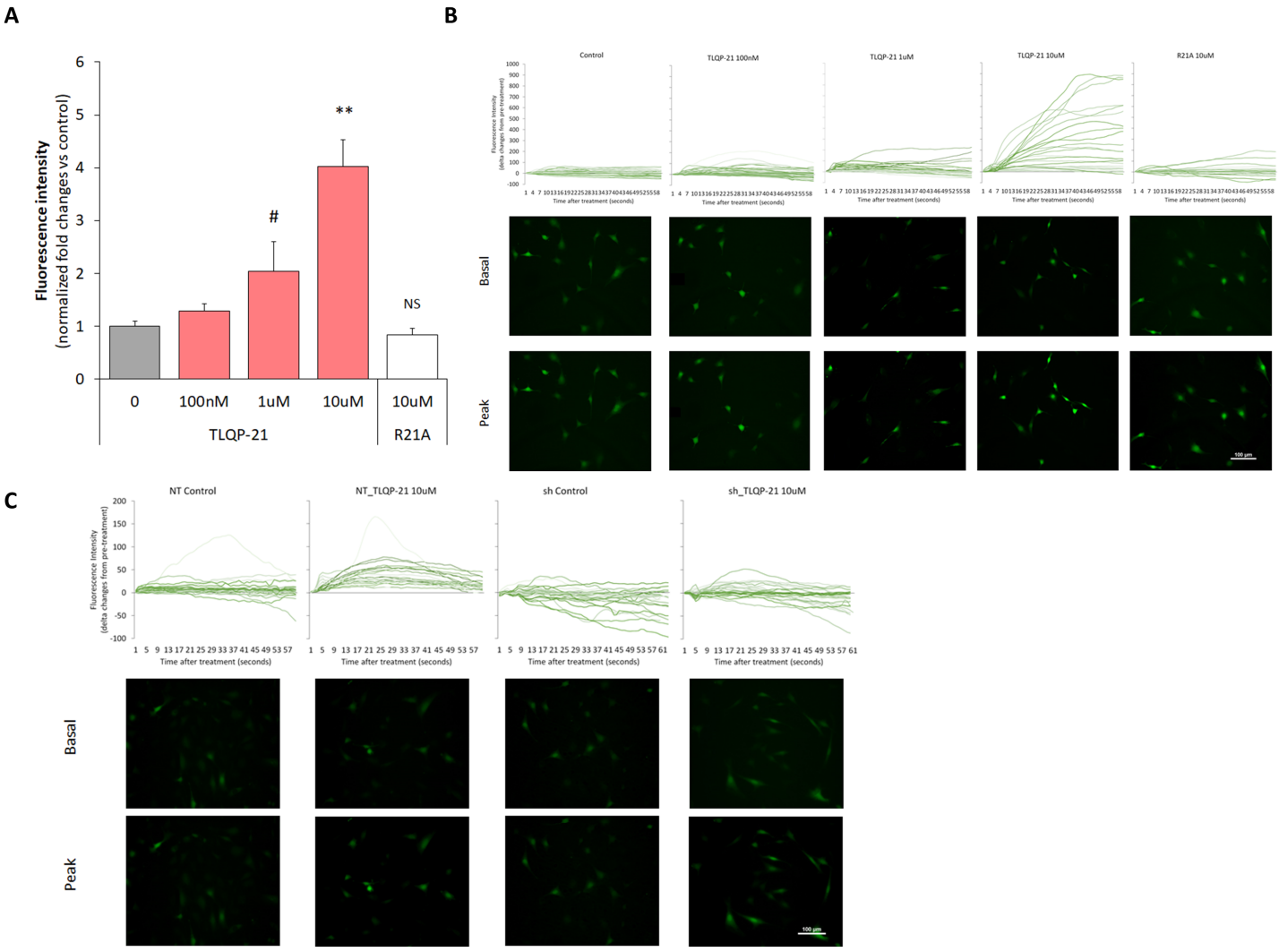

Figure S2. TLQP-21 but not the R21A mutant dose dependently increase [Ca^{2+}]i measured with Fluo-4, Related to Figure 2.. A) Area under the curve of changes in fluorescence intensity measured over 60 seconds of recording and normalized to the pre stimulation intensity ($F(1,203)=8.8$, $p<0.00001$; N=27-51 cells from 4 independent experiments). Tuckey`s post hoc tests, #$p<0.07$, *$p<0.05$, **$p<0.01$. **B**) Individual cells fluorescence intensity and representative basal and peak response for the different treatment and doses described in the figure. **C**) Individual cells fluorescence intensity and representative basal and peak response for the different treatment and doses described in not targeting shRNA control cells and C3aR1 KD cells presented in Figure 2A.

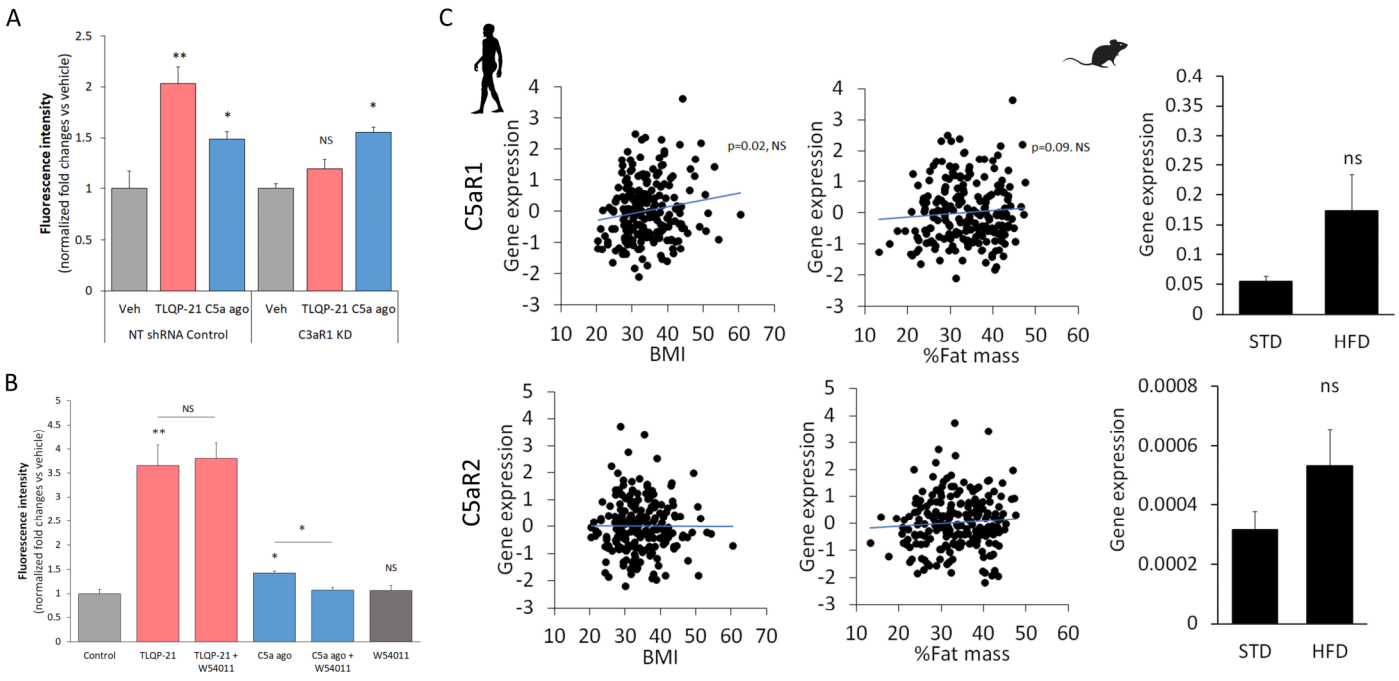

Figure S3. C3aR1 but not C5a Receptor is required for TLQP-21 activity, **Related to Figure 2 and Figure 3. A**) TLQP-21 induced but not C5a induced increase in $[Ca^{2+}]i$ is prevented by C3aR1 KD (stat). **B**) C5a but not TLQP-21 mediated increase in $[Ca^{2+}]i$. is antagonized by the C5a receptor antagonist W54011. **C**) C5aR1 and C5aR2 expression are not significantly associated with BMI (R^2: C5aR1=2.6%, C5aR2=0.0%) or %Fat Mass (R^2: C5aR1=1.4%, C5aR2=1.0%) in humans or mice.

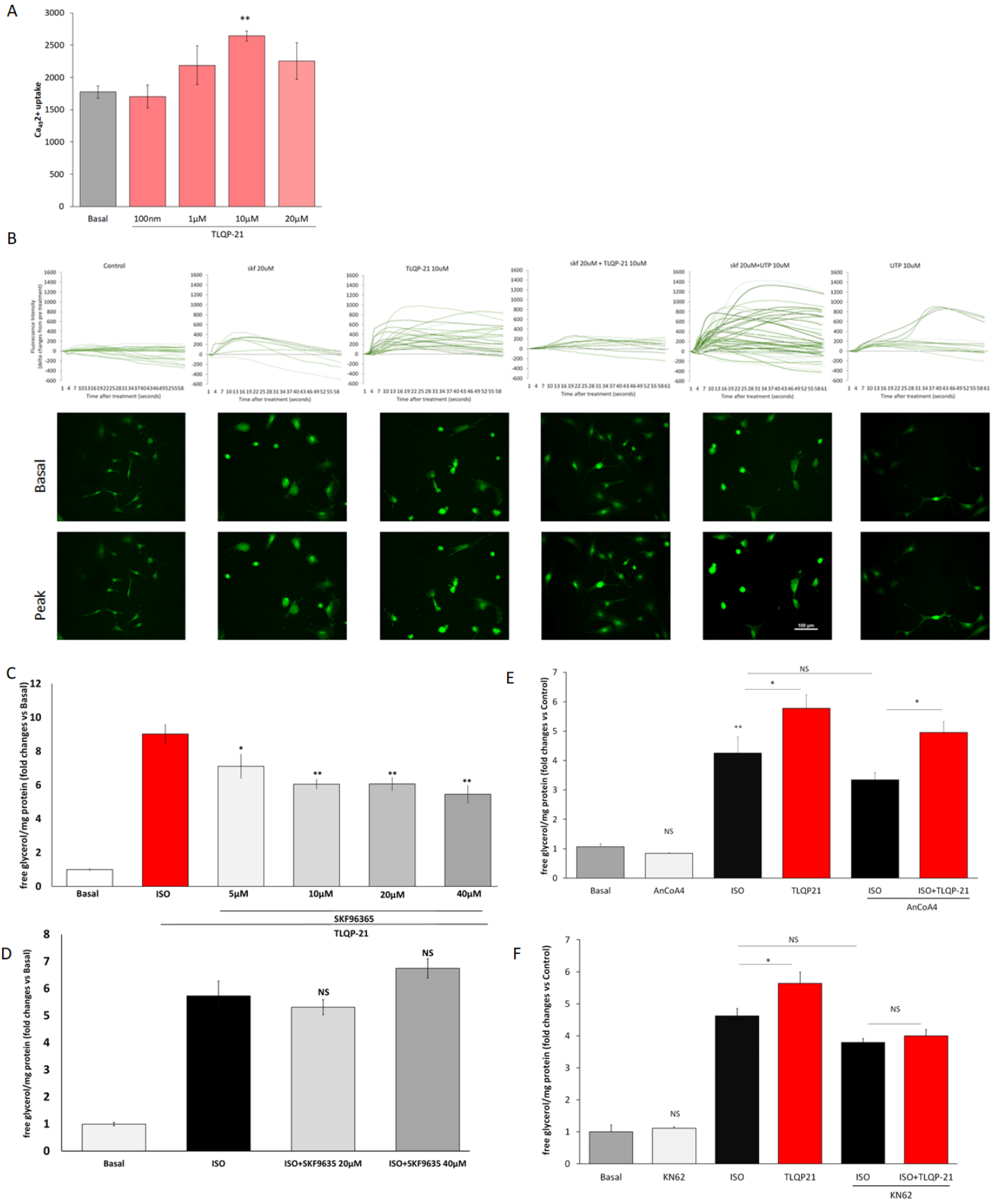

Figure S4. Title, Related to Figure 2. **A**) TLQP-21 dose-dependently increase the uptake of Ca_{45}^{2+} from the media ($F(1,20)=7.4$, $p<0.001$; N=3-9 from 3 independent experiments). **B**) Individual cells fluorescence intensity and representative basal and peak response for the different treatment (ISO, TLQP-21 or UTP) in presence or absence of the TRPC inhibitor SF-96365and doses described in not targeting shRNA control cells and C3aR1 KD cells presented in Figure 2A. **C**) SKF96365 dose-dependently inhibits

TLQP-21 potentiation of isoproterenol (ISO)-induced lipolysis. **D**) SKF96365 does not affect ISO-induced lipolysis. **E**) The Orai1 inhibitor AncoA4 does not prevent TLQP-21 potentiation of ISO induced lipolysis ($F(1,29)=65.5$, $p<0.00001$; N=3-12). **F**) The CamKII inhibitor KN62 prevents TLQP-21-induced potentiation of ISO-induced lipolysis ($F(1,18)=43.7$, $p<0.00001$; N=3-6). Tuckey`s post hoc tests, NS=not significant, *$p<0.05$, **$p<0.01$.

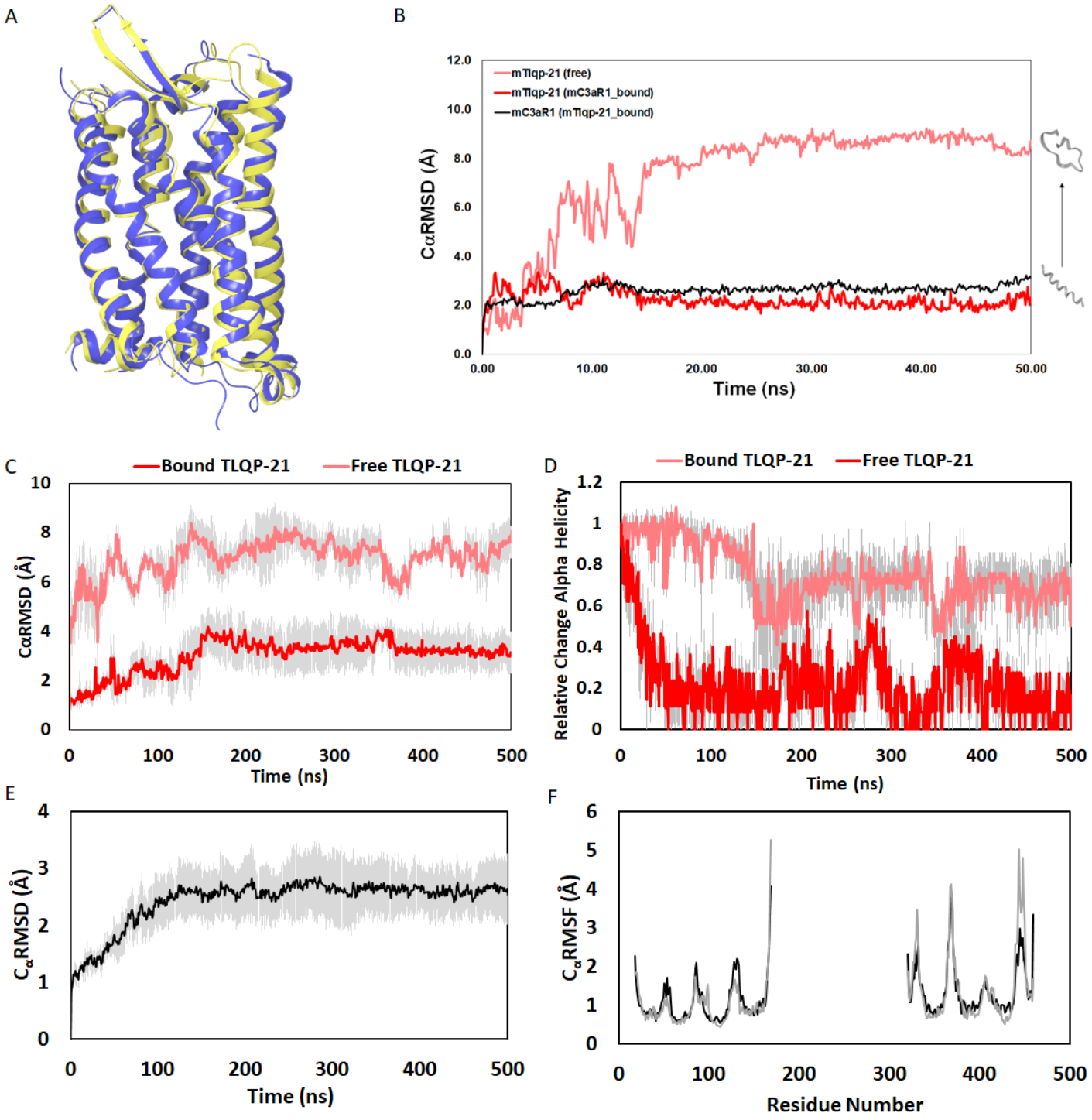

Figure S5. Structural analysis of TLQP-21 and C3aR1 interaction, Related to Figure 4. **A**) Superimposed structure by C_α atoms of two independent X-ray structure by Liu et al. 2018 (yellow; structural template of homology model) and Robertson et al., 2018 (blue). The C_αRMSD between the two structures (PDB: 5O9H and 6C1Q) was 0.87Å. The structure by Liu et al., 2018 was strategically chosen by us due to its resolved orthosteric site with bound PMX53, a cyclic peptide, for modeling of the TLQP-21 peptide. **B**) Molecular dynamics simulation of mouse (m)TLQP21 in water and in complex with mC3aR1. The CαRMSD are shown for the unbound mTLQP-21 (salmon), mC3aR1 (black) and mTLQP-21-bound mC3aR1 (red). Unbound mTLQP-21 is the same data presented in Figure 4C. The simulation showed mTLQP-21 binding to mC3aR1 retained its secondary helical structure as compared to the completely unfolded mTLQP-21 in water. **C**) Average CαRMSD of hC3aR1-bound (red) and free (pink) mTLQP-21 in solution over three 500 ns molecular dynamics simulation. Standard error reported in grey. **D**) Average relative change in alpha helicity of hC3aR1-bound (red) and free (pink) mTLQP-21 over three 500 ns MD simulation. Standard error reported in grey. **E**) Average CαRMSD of hC3aR1 with bound mTLQP-21 over three 500ns MD simulation. Standard error reported in grey. **F**) Average CαRMSF

of hC3aR1 during 50 ns (black) and 500 ns (grey) MD simulations. Gap in CαRMSF represents E2 loop not modeled in homology model.

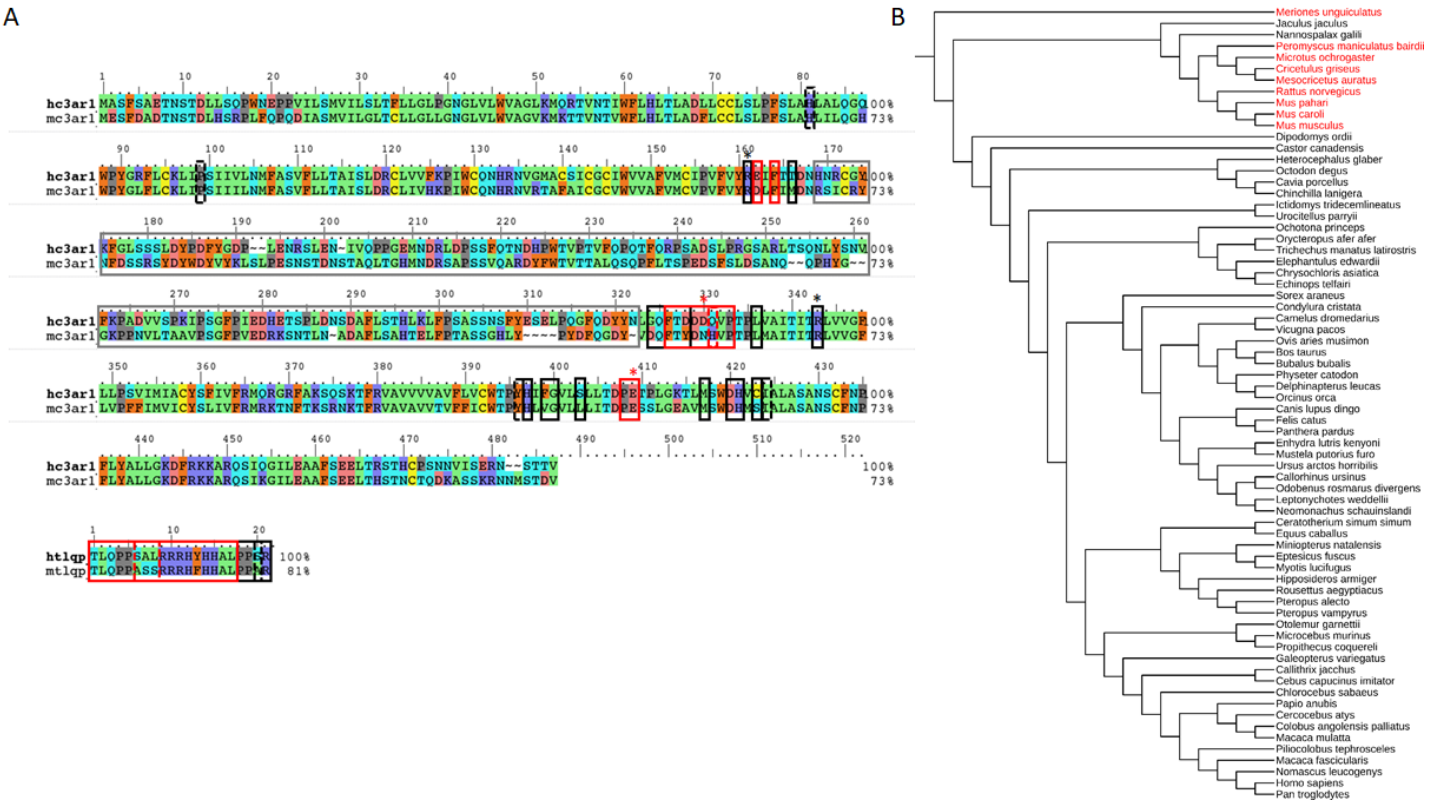

Figure S6. Sequence alignment of C3aR1 and TLQP-21, and Bayesian phylogenetic analysis of VGF, Related to Figure 4 and Table 2. **A**) Sequence alignment of the human (h) and mouse (m) C3aR1 and TLQP-21. Grey box identified the second extracellular loop. Black boxes identify the binding pocket and corresponding amino acids in the TLQP-21 identified based on our homology model. Red boxes identify amino acids interacting with the N-terminus of TLQP-21 identified based on our homology model. **B**) Bayesian phylogenetic analysis of VGF based on the 71 mammals described in the Supplementary Table 2A. We inferred the ancestral state at given position in last common ancestor of rodents, as well as last common ancestor of rodents and primates using bayesian inference in software Mr. Bayes (Ronquist et al., 2013). To this end, we first computed the gene tree using the amino-acid alignment of 71 eutherian species, including 19 rodents and 15 primates. The members of afrotheria were used as an outgroup. The sequence was partitioned to be able to retrieve ancestral states only for the positions of interest, all partitions were ran with the same model parameters (nst=1, rates=gamma). The program was run for 300 000 generations, with topological constraint to sample only trees, which include monophyletic primate and rodent clades. The probability of amino acids on the specific position was estimated based on these trees. For both nodes, the p(S)=1. Species highlighted in red express the PAR motif in TLQP-21.

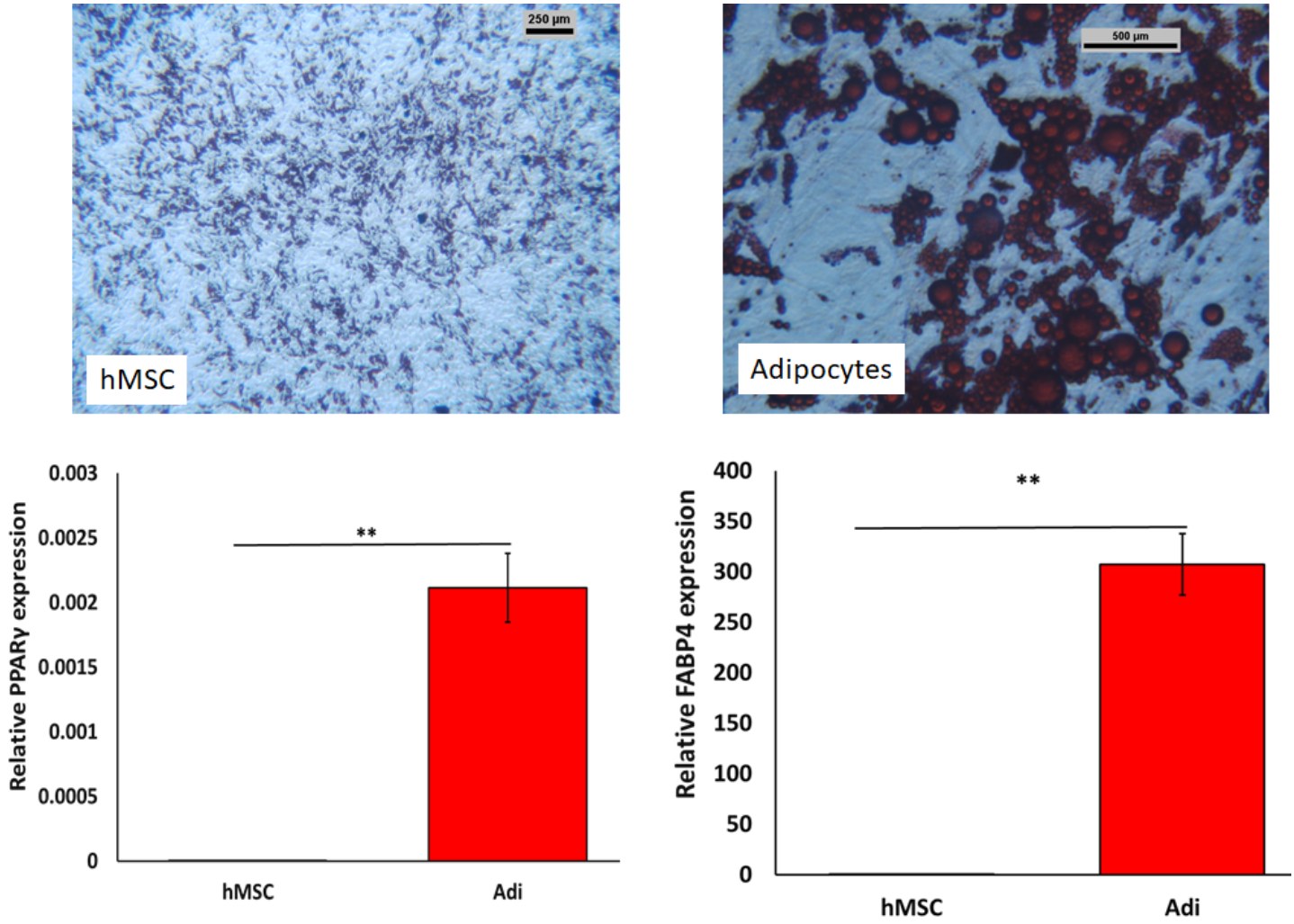

Figure S7. Characterization of human adipocytes, Related to Figure 4. Adipocytes differentiated from human mesenchymal stem cells (hMSC) manifest increased Oil-red-O staining (representative images) and increased expression of key adipogenesis markers such as PPARγ and FABP4. **p<0.00001.

Table S1. Oligonucleotides used in this study, Related to STAR Methods

GENE NAME	SPECIES	FORWARD SEQUENCE 5'-3'	REVERSE SEQUENCE 5'-3'
ATGL	Mouse	CCACGCCACTCACATCTACGG	TCACCAGGTTGAAGGAGGGAT
ADBR1	Mouse	CTCATCGTGGTGGGTAACGTG	ACACACAGCACATCTACCGAA
ADBR2	Mouse	GGGAACGACAGCGACTTCTT	GCCAGGACGATAACCGACAT
ADBR3	Mouse	CCAGCCAGCCCTGTGGA	GGACGCGCACCTTCATAGC
Beta actin	Mouse	GGC ACC ACA CCT TCT ACA ATG	GGG GTG TTG AAG GTC TCA AAC
C3aR1	Mouse	TCGATGCTGACACCAATTCAA	TCCCAATAGACACCAATTCAA
HSL	Mouse	GCTGGTGCAGAGAGACAC	GAAAGCAGCGCGCACGCG
Trpc1	Mouse	GTCGCACCTGTTATTTTAGCTGC	TGGGCAAAGACACATCCTGC
Leptin	Mouse	CAGGGAGGAGGAAAATGTGCTGGAG	CCGACTGCGTGTGTGAAATGTC
PPAR-gamma	Mouse	GTGCCAGTTTCGATCCGTAGA	GGCCAGCATCGTGTAGATGA
C5aR1	Mouse	CAGGCGGTGTAGAGGAGAAG	GAAGGAAGGAAGGAGGAGAGG
C5aR2	Mouse	CTGGGCCTCTTGCTGACTGTGC	GCCCCAGGAAGCCAAAGAGGA
PPAR-gamma	Human	ACTCTGGGAGATTCTCCTATT	CTCCATAGTGAAATCCAGAAG
FABP-4	Human	ACTGGGCCAGGAATTTGACGAAGT	TCTCGTGGAAGTGACGCCTTTCAT
C5aR1	Human	GCTGACCATACCCTCCTTCCT	CCGTTTGTCGTGGCTGTAGTC
C5aR2	Human	TGCTGTTTGTCTCTGCCCATC	GTCAGCAGGATGATGGAGGG
C3aR-V103I	Human	GCTGATACCCTCCATCATAATCCTTAATATGTTTG	GACGGATGCAAACATATTAAGGATTATGATGGAGGG
C3aR-S400L	Human	CTTATCACATCTTTGGAGTGCTGTTGCTGCTGACCG	GTTTCGGGATCGGTCAGCAGCAACAGCACTCCAAAGATG
C3aR-L413V	Human	CCCCTCTCGGGAAGACCGTTATGTCTTGGGATC	GTGATCCCAAGACATAACGGTCTTCCCGAGAGG
C3aR-V419M/C420S	Human	GTCTTGGGATCACATGTCCATCGCCCTTGCCAGCGCC	CAAGAATTGGCGCTGGCAAGGGCGATGGACATGTGATCCCAAG